Magnetic structure and magnetoelectric properties of the spin-flop phase in LiFePO4

Sofie Holm-Janas, Mitsuru Akaki, Ellen Fogh, Takumi Kihara, Manh Duc Le, Paola Catarina Forino, Stanislav E. Nikitin, Tom Fennell, Adheena Painganoor, David Vaknin, Masao Watanabe, Niels Bech Christensen, Hiroyuki Nojiri, and Rasmus Toft-Petersen

Published version information

Citation: Sofie Holm-Janas (et.al.) Magnetic structure and magnetoelectric properties of the spin-flop phase in LiFePO4, Phys. Rev. B 109, 174413

DOI: https://doi.org/10.1103/PhysRevB.109.174413

Editors' Suggestion

Magnetic structure and magnetoelectric properties of the spin-flop phase in $LiFePO_4$

Sofie Holm-Janas,[1] Mitsuru Akaki,[2] Ellen Fogh,[3] Takumi Kihara,[2,4] Manh Duc Le,[5] Paola Catarina Forino,[1,3] Stanislav E. Nikitin,[6] Tom Fennell,[6] Adheena Painganoor,[1,7] David Vaknin,[8] Masao Watanabe,[9] Niels Bech Christensen,[1] Hiroyuki Nojiri,[2] and Rasmus Toft-Petersen[1,10,*]

[1]*Department of Physics, Technical University of Denmark, 2800 Kongens Lyngby, Denmark*
[2]*Institute for Materials Research, Tohoku University, Sendai 980-8577, Japan*
[3]*Laboratory for Quantum Magnetism, Institute of Physics, École Polytechnique Fédérale de Lausanne (EPFL), 1015 Lausanne, Switzerland*
[4]*Research Institute for Interdisciplinary Science, Okayama University, Okayama, 700-8530, Japan*
[5]*ISIS Neutron and Muon Source, Rutherford Appleton Laboratory, Didcot OX11 0QX, United Kingdom*
[6]*Laboratory for Neutron Scattering and Imaging, Paul Scherrer Institut, 5232 Villigen PSI, Switzerland*
[7]*Institut Laue-Langevin, 71 avenue des Martyrs, CS 20156, Grenoble, 38042 Cedex 9, France*
[8]*Ames National Laboratory and Department of Physics and Astronomy, Iowa State University, Ames, Iowa 50011, USA*
[9]*Materials and Life Science Division, J-PARC Center, Tokai, Ibaraki 319-1195, Japan*
[10]*European Spallation Source ERIC, P.O. Box 176, SE-221 00, Lund, Sweden*

(Received 11 March 2024; accepted 18 April 2024; published 6 May 2024)

We investigate the magnetic structure and magnetoelectric(ME) effect in the high-field phase of the antiferromagnet $LiFePO_4$ above the critical field of 31 T. A neutron diffraction study in pulsed magnetic fields reveals the propagation vector to be $\mathbf{q} = 0$ for the high-field magnetic structure. Pulsed-field electric polarization measurements show that, at the critical field, the low-field off-diagonal ME coupling α_{ab} is partially suppressed, and the diagonal element α_{bb} emerges. These results are consistent with a spin-flop transition where the spin direction changes from primarily being along the easy b axis below the transition to being along a above. The persistence of off-diagonal ME tensor elements above the critical field suggests a lowering of the magnetic point-group symmetry and hence a more complex magnetic structure in the high-field phase. In addition, neutron diffraction measurements in low magnetic fields show no observable field-induced spin canting, which indicates a negligible Dzyaloshinskii-Moriya interaction. The observed spin-flop field supports the Hamiltonian recently deduced from inelastic neutron studies and indicates that the system is less frustrated and with a larger single-ion anisotropy than originally thought. Our results demonstrate the effectiveness of combining pulsed-field neutron diffraction and electric polarization measurements to elucidate the magnetic structures and symmetries at the highest attainable field strengths.

DOI: 10.1103/PhysRevB.109.174413

I. INTRODUCTION

Multiferroics and magnetoelectric (ME) materials carry the prospect for applications, such as electrical-field control of skyrmions and low-power-consumption logic devices [1–6]. To date, the vast majority of realized devices adopts alternating layers, e.g., of piezoelectric and magnetostrictive materials, where the mechanical coupling between layers creates an artificial ME material with the desired functionality. However, some of these innovative designs employ distinct ME layers, and a fundamental understanding of single-phase MEs is crucial for progress in the field. The allowed ME coupling tensor elements α_{ij} between an applied magnetic field H_j and electric polarization $P_i = \alpha_{ij}H_j$ are dictated by the magnetic point-group symmetry [7]. In this respect, the magnetic phase diagrams of ME materials serve as testing grounds for model spin Hamiltonians since distinct ME coupling tensors may be realized within the same compound by temperature and magnetic-field control of the ground state [8,9].

The lithium orthophosphates are a well-studied family of orthorhombic ME materials [10] of chemical formula $LiMPO_4$ (M = Mn, Fe, Co, Ni), all ordering antiferromagnetically(AFM) below Néel temperatures in the range T_N = 20–50 K [11–18]. The single-ion anisotropy in the system depends on the transition metal ion M in question. Thus, different magnetic point-group symmetries are realized in the AFM ground state depending on M, which in turn results in different ME tensor forms [10,19,20]. Two mechanisms for the physical origin of the ME coupling have been proposed in this class of materials, based on exchange striction [21–24] and orbital magnetism [25].

$LiFePO_4$, the focus of this paper, orders with spins predominantly along the easy b axis below $T_N = 50$ K with intermediate axis a and hard axis c [17]. The zero-field magnetic ground state has been determined in detail (see Sec. II) and has a lower symmetry than what was initially expected. This may be explained by a recent observation of strong magnetostriction peaking at T_N in $LiFePO_4$, as measured by

*rasp@fysik.dtu.dk

dilatometry [26]. The excitations have been investigated in great detail using both neutron spectroscopy [8,12,23], electron spin resonance (ESR) spectroscopy [27], and terahertz absorption spectroscopy [28]. Recently, the latter revealed a veritable zoo of excitations, including electromagnons and other ME active modes [28]. Extensive work on modeling the exchange interactions and single-ion anisotropy constants of $LiFePO_4$ has been undertaken [8,20,23,27,28]. While the different models agree on the order of magnitude of the interactions, the level of exchange frustration in $LiFePO_4$ is debated.

Neutron spectroscopy measurements reveal mild exchange frustration in all the different lithium orthophosphates [15,16,23,29]. The competition between exchange and single-ion anisotropy governs the magnetic phase diagrams, which vary in complexity for the different family members [8,15,18,20,21,26,30,31]. The Mn analog $LiMnPO_4$ has the simplest phase diagram with a spin-induced transition to an incommensurate, elliptic spin cycloid at ∼12 T applied magnetic field [13]. This is followed by a spin-flop transition at higher magnetic fields, where the system becomes commensurate again. $LiNiPO_4$, on the other hand, first exhibits a spin-density phase upon cooling down in zero field before entering the AFM ground state at low temperatures. Upon applying a magnetic field, $LiNiPO_4$ undergoes a succession of transitions between commensurate and incommensurate phases. Intriguingly, in $LiNiPO_4$, the same ME coupling tensor α_{ij} is observed in the high-field commensurate phases as in zero field. These phases also have the same $\mathbf{q} = 0$ propagation vector, which indicates that the high-field commensurate phases are magnetized variants of the zero-field commensurate phase rather than a spin-flop phase.

The behavior of $LiFePO_4$ differs somewhat from these two sister compounds. From the similarity of the XY-like anisotropy in $LiFePO_4$ to that of $LiNiPO_4$, one might also expect to observe incommensurate (spiral or spin-density wave) phases in $LiFePO_4$. However, unlike $LiNiPO_4$, with its multiple phase transitions as a function of magnetic field, magnetization measurements on $LiFePO_4$ reveal only a single clear field-induced phase transition at $\mu_0 H \simeq 32$ T [26], demonstrating the robustness of the zero-field structure against the application of a magnetic field. The transition is speculated to be of the spin-flop type, but this has not yet been verified experimentally [26–28].

In this paper, we combine neutron diffraction and electric polarization measurements, both performed with pulsed magnetic fields, to determine the high-field magnetic structure in $LiFePO_4$. We find the phase transition at 31 T to be of the spin-flop type with spins reorienting to point dominantly along the a axis. However, the high-phase ME tensor components imply a more complex magnetic structure than a colinear AFM structure with magnetic moments oriented along the a axis. Furthermore, in a different neutron diffraction experiment, we find no further field-induced spin canting, which indicates a negligible Dzyaloshinskii-Moriya (DM) interaction. Finally, we perform mean-field(MF) calculations to determine the phase diagram based on previously estimated sets of exchange parameters to compare with the experimentally obtained phase diagram and find that the less frustrated set of exchange parameters, with larger spin anisotropies, provide a better description of all data. This demonstrates that studies of magnetic phase diagrams are complementary to studies of magnetic excitations, when the magnetic Hamiltonian is complex.

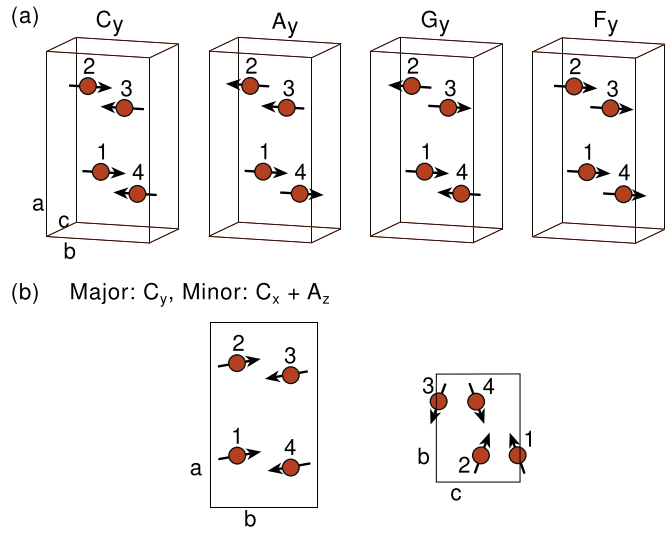

FIG. 1. (a) The basis vectors of LiMPO$_4$ for $\mathbf{q} = 0$ structures in the *Pnma* space group. Only the lattice of magnetic ions is shown. The arrows represent the spin orientation on the four magnetic sites labeled 1–4 as shown. (b) Projections onto the (b, c) and (a, b) planes for the zero-field magnetic structure of $LiFePO_4$, $[C_y + C_x + A_z]$. Canting angles are exaggerated for clarity.

II. MAGNETIC STRUCTURES AND THE ME TENSOR

The crystal structure of the lithium orthophosphates has historically been assumed to belong to the *Pnma* space group [11]. The four Fe^{2+} ions are located on the Wyckoff position $4c$: $\mathbf{r}_1 = (\frac{1}{4} + x, \frac{1}{4}, -z)$, $\mathbf{r}_2 = (\frac{3}{4} + x, \frac{1}{4}, \frac{1}{2})$, $\mathbf{r}_3 = (\frac{3}{4} - x, \frac{3}{4}, z)$, and $\mathbf{r}_4 = (\frac{1}{4} - x, \frac{3}{4}, \frac{1}{2} - z)$, where $x = 0.03$ and $z = 0.025$ in the orthorhombic unit cell [23]. The spin structure can be described by the four irreducible basis vectors: $A = (\uparrow\downarrow\downarrow\uparrow)$, $C = (\uparrow\uparrow\downarrow\downarrow)$, $G = (\uparrow\downarrow\uparrow\downarrow)$, and $F = (\uparrow\uparrow\uparrow\uparrow)$. Here, $\uparrow$ and $\downarrow$ denote the relative orientation of the four spins in a unit cell which are enumerated 1–4, see Fig. 1(a). The four basis vectors combined with magnetic moment orientations along the three perpendicular crystallographic axes (a, b, and c) then allow for a full description of the magnetic structures. There are eight irreducible representations (IRs) for *Pnma*, denoted Γ_i for $i = 1, \ldots, 8$, see. e.g.. Ref. [23]. Only some of these are realized in the lithium orthophosphates. The main magnetic structure element for all the compounds in the lithium orthophosphate family is of C type with major spin components along either a ($LiMnPO_4$), b ($LiCoPO_4$ and $LiFePO_4$), or c ($LiNiPO_4$), see Table I for a summary.

The ME properties depend intimately on the magnetic point group in the ordered ground state. Of all the 122 possible magnetic point groups, only 58 allow the linear ME effect. The specific point-group symmetry dictates the form of the ME tensor, see, e.g., Ref. [7]. The resulting ME tensor for the point groups relevant to the lithium orthophosphates are listed in Table I.

TABLE I. IRs for the *Pnma* space group and the allowed tensor forms for the linear ME effect in the lithium orthophosphates. The first two columns list the IR(s), the second column gives the point group symmetry, andthe third the ME tensor form. Small dots indicate vanishing tensor elements, and large dots show elements that may be finite. The last column specifies which (if any) lithium orthophosphate displays the corresponding low-temperature, zero-field structure.

IR No. 1	IR No. 2	Point group	ME tensor	Compound
$\Gamma_5(C_x, A_z)$		$m'm'm'$	$\begin{pmatrix} \bullet & \cdot & \cdot \\ \cdot & \bullet & \cdot \\ \cdot & \cdot & \bullet \end{pmatrix}$	$LiMnPO_4$
$\Gamma_7(C_z, A_x)$		$mm'm$	$\begin{pmatrix} \cdot & \cdot & \bullet \\ \cdot & \cdot & \cdot \\ \bullet & \cdot & \cdot \end{pmatrix}$	$LiNiPO_4$
$\Gamma_8(C_y)$		mmm'	$\begin{pmatrix} \cdot & \bullet & \cdot \\ \bullet & \cdot & \cdot \\ \cdot & \cdot & \cdot \end{pmatrix}$	
$\Gamma_8(C_y)$	$\Gamma_5(C_x, A_z)$	$2_z/m'_z$	$\begin{pmatrix} \bullet & \bullet & \cdot \\ \bullet & \bullet & \cdot \\ \cdot & \cdot & \bullet \end{pmatrix}$	$LiFePO_4$
				$LiCoPO_4$
$\Gamma_5(C_x, A_z)$	$\Gamma_7(C_z, A_x)$	$2_y/m'_y$	$\begin{pmatrix} \bullet & \cdot & \bullet \\ \cdot & \bullet & \cdot \\ \bullet & \cdot & \bullet \end{pmatrix}$	
$\Gamma_8(C_y)$	$\Gamma_7(C_z, A_x)$	$2'_x/m_x$	$\begin{pmatrix} \cdot & \bullet & \bullet \\ \bullet & \cdot & \cdot \\ \bullet & \cdot & \cdot \end{pmatrix}$	

It was previously shown that the dominant component of the magnetic structure of $LiFePO_4$ is C_y but that there are additional subdominant components C_x and A_z corresponding to the spins rotating off the crystallographic b axis. The refined moment along the b axis is $\mu_y = 4.09(4)\,\mu_B$ (from the C_y component), while the refined canted moments are $\mu_x = 0.067(5)\,\mu_B$ along the a axis and $\mu_z = 0.063(5)\,\mu_B$ along the c axis, corresponding to an overall rotation of $1.3(1)^\circ$ off the b axis [23]. The structure is shown in Fig. 1(b) with exaggerated canting angles [23].

The major component C_y belongs to the Γ_8 IR under the *Pnma* space group. The minor components C_x and A_z belong to Γ_5, meaning that two different IRs are involved, and hence, the magnetic point-group symmetry is lowered from mmm' (purely Γ_5) to $2_z/m'_z$ ($\Gamma_5 \otimes \Gamma_8$). This in turn relaxes the constraints on the ME tensor (Table I). Indeed, a recent study of the ME couplings at low fields found a weak but finite signal corresponding to the diagonal element α_{aa} [22], consistent with $2_z/m'_z$ symmetry. This highlights the strength in using the ME coupling tensor to support magnetic structure determination and indicates that the crystal structure of $LiFePO_4$ at zero field is of lower symmetry than *Pnma* [23].

In Ref. [26], a spin flop was suggested at the 31 T transition. Assuming that the symmetry of the dominant structure component remains C, the ME tensor form above the critical field would follow that of point group $m'm'm'$ (C_x) or $mm'm$ (C_z). Given that the c axis is the hard axis of $LiFePO_4$, it seems most likely that the system would flop to a structure dominated by C_x. For a structure exclusively described by the C_x basis vector, one would expect the ME tensor to change to contain only finite diagonal elements (α_{ii}, $i = a, b, c$), while a structure involving a linear combination of sizable C_x and C_z would also give rise to finite off-diagonal elements (α_{ab} and α_{ba}) in addition to the diagonal elements (cf. Table I).

III. EXPERIMENTAL DETAILS

$LiFePO_4$ single crystals were grown via the standard flux growth technique, using LiCl as the flux and a stoichiometric mixture of high-purity $FeCl_2$ and Li_3PO_4. The composition and structure were confirmed via x-ray powder diffraction (XRD) [12].

To probe the structure of the high-field phase with neutron diffraction, pulsed magnetic fields are required to reach sufficiently elevated fields. Neutron diffraction in pulsed magnetic fields has become an established technique within the last decade [32–39] and was already used to elucidate the field-induced phases in $LiNiPO_4$ [21,39]. However, the low duty cycle of the magnet coils and the resulting long counting times as well as the limited scattering geometry imposed by the coils present a number of experimental challenges linked to this technique. To align the magnet and neutron pulse, the time delay Δt between the two pulses must be adjusted such that the maximum field coincides with the desired scattering vector **Q**. The principle of the technique is illustrated in Fig. 2. So far, these pulsed-field experiments have all been performed in forward-scattering geometry [21,32–39]. In the case at hand, however, it is necessary to probe scattering vectors **Q** parallel to the field **H**, i.e., **Q** || **H**, which for solenoids can only be done in backscattering geometry. This was challenging for a number of reasons. First, longer wavelengths are needed in backscattering than forward scattering for any given **Q**. The Japan Proton Accelerator Research Complex (J-PARC) moderator has lower brilliance at these wavelengths [40]. In addition, the Q range covered in the time span of a field pulse is significantly smaller in backscattering geometry, necessitating many different field settings and hence many more magnet pulses to cover the desired region in ($\mathbf{Q}, H$) than experiments performed in forward scattering.

To directly probe the magnetic structure of $LiFePO_4$ at high magnetic fields, a time-of-flight (ToF) neutron Laue diffraction experiment was performed at NOBORU, the Neutron Source Diagnostic & Test Port, at J-PARC [40]. A pulsed polychromatic neutron beam was incident on the sample and the scattered neutrons captured by a position sensitive area detector. The detector was operated in integration mode with a 30 µs bin size. The pulsed magnetic field was generated by recently developed wide-angle magnet coils with a maximum field strength of $B_{\max} = 35$ T and pulse duration of 5 ms [41]. The coils have maximum and minimum scattering angles 2θ of 42° and 138°, for forward and backwards scattering, respectively. The coil is immersed in liquid nitrogen. The sample in vacuum was attached to a 7-diameter single-crystalline sapphire rod connected to a closed-cycle refrigerator with a base temperature of 4.5 K.

A 60 mg ($2.6 \times 2.2 \times 3.0$ mm^3) single crystal was oriented with the crystallographic b axis (easy axis) parallel to the direction of the applied magnetic field and with $\mathbf{Q} = (HK0)$ in

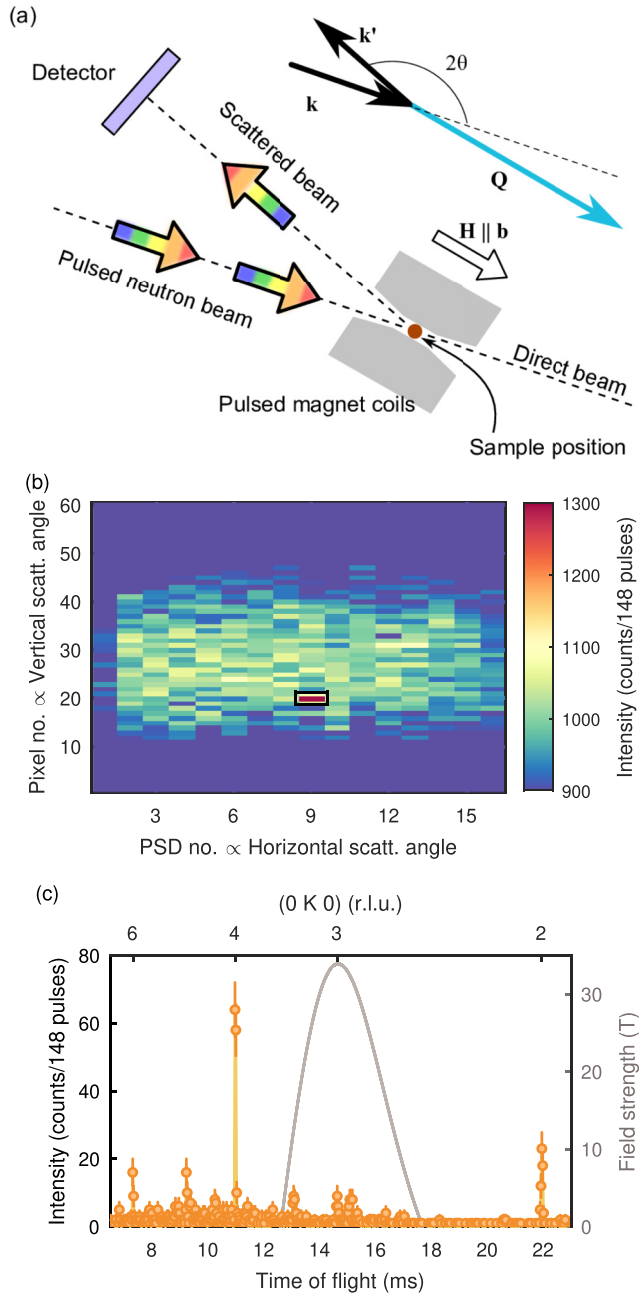

FIG. 2. (a) Schematic of the neutron Laue diffraction backscattering setup at NOBORU. The incoming beam is polychromatic with wave vector $\mathbf{k}$, scattered wave vector $\mathbf{k}'$, and scattering vector $\mathbf{Q} = \mathbf{k} - \mathbf{k}'$. The pulsed magnet coils (gray) allow a maximum $2\theta = 42^\circ$. The magnetic field is parallel to the b axis of the sample. (b) Position-sensitive detector image for a pulsed-field measurement. The detector has 16 vertical tubes, each with 60 pixels. The color represents the neutron intensity integrated over 148 pulses and all neutron flight times. The high-intensity pixel enclosed in the black rectangle corresponds to neutron momentum transfers along $\mathbf{Q} = (0K0)$. (c) Neutron intensity vs time of flight for the high-intensity pixel shown in (b). The top axis shows the corresponding value of K along $\mathbf{Q} = (0K0)$. The magnetic field strength (gray line) is indicated on the right-hand axis. The time delay between the neutron and magnet pulse has been adjusted to reach the maximum field strength of 34 T at $\mathbf{Q} = (030)$.

the horizontal scattering plane, see Fig. 2. This setup allowed us to reach momentum transfers along $(0K0)$ in backscattering geometry. The ToF can be converted to $\mathbf{Q} = (0K0)$ following $K = 2\alpha L \sin\theta/\mathrm{ToF}$, where $\alpha = 252.7\,\mu\mathrm{s\,m^{-1}\,\AA^{-1}}$, θ is half the scattering angle, and $L = 14.9\,\mathrm{m}$ is the distance from the neutron target via the sample position to the detector.

Electric polarization measurements with pulsed magnetic fields were performed at the Institute for Materials Research, Tohoku University. The samples used for these measurements were three $LiFePO_4$ single-crystalline plates of size $\sim 1 \times 1 \times 0.5\ \mathrm{mm}^3$, which were cut from the same crystal as used for neutron diffraction. They were aligned within 5° with respect to the magnetic field direction. The pulsed-field coil delivered a field pulse with a total duration of 6.3 ms. The magnet pulse is split into two parts, each with a full with at half maximum (FWHM) time length of 2.1 ms. In the first part, the maximum field is reached at 35 T followed by an opposing pulse of magnitude 21 T. See Appendix B for details.

We probed each combination of directions of electric polarization and magnetic fields, here denoted by P_iH_j, where $\{i, j\} = \{a, b, c\}$. The measurement procedure was as follows: For each P_iH_j, the sample was cooled down to base temperature of 4.2 K in zero applied magnetic field. Note that no poling was possible with this setup. The electric polarization was then measured during a magnetic field pulse at consecutively increasing temperatures. During such a measurement series, it is assumed that the sample remained in the same domain state. However, for repeated measurements, we observed a slight shift in the measured polarization, likely due to the system settling into a different domain state upon the initial cooling below T_N. The consequence is that temperature and field dependencies may be regarded as reliable within a single measurement series, but absolute values of the electric polarization will vary between separate datasets. Data collected at 60 K were used for background subtraction (except for P_bH_c).

To obtain an estimate for the size of the DM interaction, neutron diffraction with static magnetic fields was performed at the thermal triple-axis spectrometer EIGER at SINQ at the Paul Scherrer Institute [42]. EIGER was operated in elastic mode with incoming and outgoing energy $E = 14.64\,\mathrm{meV}$, and $40'$ collimation both before and after the sample. A pyrolytic graphite filter was placed between the sample and the analyzer to suppress higher-order scattering. Two different experiments were performed, one with magnetic field along the a axis and another along the c axis. The first experiment with $\mathbf{H}||\mathbf{a}$ was performed on the same 30 mg single-crystal as used at NOBORU. It was aligned with $(0KL)$ in the horizontal scattering plane and placed in a vertical ^{4}He cryomagnet with a maximum field of 12 T. The second experiment with $\mathbf{H}||\mathbf{c}$ was performed on a 140 mg single-crystal aligned with $(HK0)$ in the horizontal scattering plane and placed in a vertical ^{4}He cryomagnet with a maximum field of 10 T.

IV. RESULTS

A. Magnetic structure in the high-field phase

The intensity of a Bragg reflection depends on the nuclear and magnetic structure. The intensity arising from the magnetic structure is proportional to the neutron magnetic

TABLE II. Squared structure factors (F^2) and polarization factors (P^2) and nuclear structure factors for selected Bragg reflections in $LiFePO_4$, see Eqs. (1)–(4).

q	$\|F_C\|^2$	$\|F_A\|^2$	$\|F_G\|^2$	$\|F_F\|^2$	$\|F_N\|^2$	$\|P_x\|^2$	$\|P_y\|^2$	$\|P_z\|^2$
(020)	0	0	0	16	5300	1	0	1
(030)	16	0	0	0	0	1	0	1

scattering cross-section:

$$I^{\mathrm{Mag}}(\mathbf{q}) \propto f(\mathbf{q})^2 \sum_R \langle S_R\rangle^2 |F_R(\mathbf{q})|^2 \sum_i |P_i(\mathbf{q})|^2, \quad (1)$$

where $f(\mathbf{q})$ is the ion-dependent magnetic form factor, and $\langle S_R\rangle$ is the thermal average of the magnetic moment for the structure $R = \{A, G, C, F\}$, as explained in Sec. II. The magnetic structure is represented through the squared magnetic structure factor $|F_R(\mathbf{q})|^2$ and spin polarization $|P_i(\mathbf{q})|^2$ for $i = \{x, y, z\}$, which are defined as

$$F_R(\mathbf{q}) = \sum_d \mathbf{m}_d^R \exp(i\mathbf{q}\cdot\mathbf{r}_d), \quad (2)$$

$$\mathbf{P}(\mathbf{q}) = \mathbf{q}\times(\hat{\mathbf{e}}\times\mathbf{q}). \quad (3)$$

Here, $\mathbf{m}_d^R$ is the magnetic moment at site $d = 1, ..4$ for the structure R, and $\hat{\mathbf{e}}$ is the unit vector for directions $\{x, y, z\}$. The intensity arising from the nuclear structure is proportional to the nuclear structure factor:

$$F_N(\mathbf{q}) = \sum_j b_j \exp(i\mathbf{q}\cdot\mathbf{r}_j), \quad (4)$$

where the sum runs over all j atoms in the unit cell (both magnetic and nonmagnetic) with scattering length b_j at position $\mathbf{r}_j$. Table II shows the squared structure and polarization factors for a few selected magnetic Bragg reflections for the different possible structures R. Note that, while a given reflection may have a finite structure factor for a specific basis vector, the intensity can still be vanishing due to the polarization factor.

Figure 3(a) shows the diffraction data obtained in zero field at 4.5 K. The nuclear Bragg reflections are identified as the high-intensity peaks and indicated in the figure. These are present at all applied fields and are a good indication that the sample stayed in position for the duration of the experiment. Lower-intensity peaks are observed in the region $6-16$ ms [corresponding to $K = 2.5-6$ in $\mathbf{Q} = (0K0)$], stemming from aluminum and copper in the sample environment, see Appendix A for a detailed treatment.

Data combined from 148 magnet pulses collected at 4.5 K and with $B_{\max} = 34$ T are shown in Fig. 3(b) together with the scaled zero-field measurement. The high-field data clearly contain a peak at $\mathbf{Q} = (030)$, which is not present in the zero-field phase to be commensurate with propagation vector $\mathbf{q} = 0$. To understand the further implications of this new magnetic signal, we turn to Table II. The (030) Bragg peak has finite neutron intensity exclusively for a C-type structure with spins oriented along either the a or c axis.

Due to the low flux and the backscattering geometry, the pulsed-field setup employed here is unable to detect weak magnetic Bragg peaks. The observed (030) peak is ~2.5 times weaker than the strong nuclear (020) reflection, demonstrating the ordered C_x moment to be of a similar order of magnitude to the zero-field C_y component and therefore likely the main structural component.

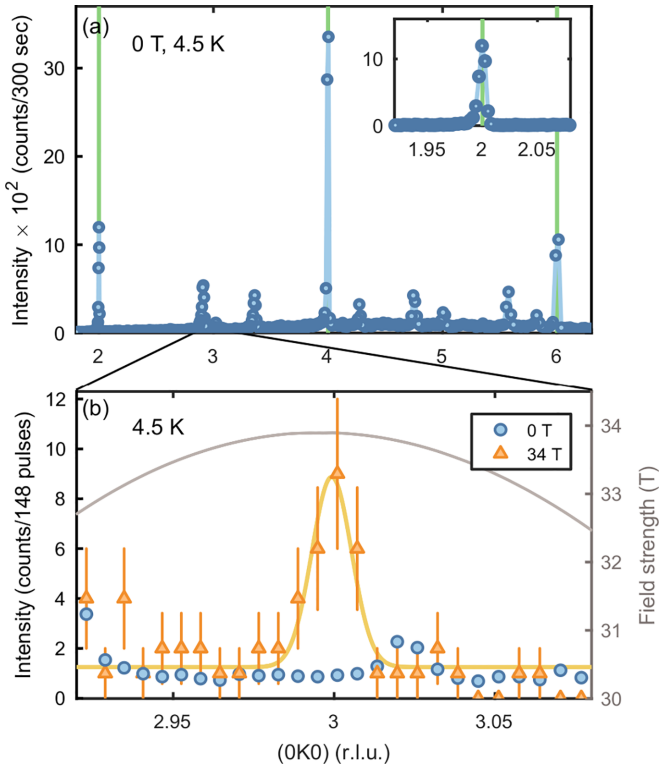

FIG. 3. Neutron diffraction measurement of $LiFePO_4$ with pulsed magnetic fields. (a) Diffraction intensity as a function of K along $\mathbf{Q} = (0K0)$ in zero applied magnetic field. Green lines indicate nuclear Bragg reflections. Inset focuses on the (020) reflection. (b) Diffraction intensity along $\mathbf{Q} = (0K0)$ in pulsed magnetic fields. Zero-field data from (a) has been scaled to use as background. A Gaussian (yellow) line has been fitted to the pulsed-field data as a guide to the eye of the (030) reflection. The strength of the magnetic field pulse is shown on the right-handside in gray.

B. The magnetoelectric effect

Figure 4(a) shows all nine combinations of the electric polarization along i induced in applied magnetic field along j, P_iH_j, $\{i, j\} = \{a, b, c\}$, at different temperatures. The ME coefficients α_{ij} may be extracted from the slopes of P_i as a function of H_j. Three nonzero tensor elements are observed: For fields along a, a linear ME effect is seen for P_b for all field strengths and temperatures, while the other polarization components are zero. For fields along b, a clear phase transition takes place at $B_{\mathrm{SF}} = 31 \pm 1$ T and 4.2 K, where P_a of the low-field phase shows a dip, and simultaneously, P_b appears. This value of the transition field is in accordance with previous observations [26,28,43]. For fields along c, no ME signals are observed within the experimental sensitivity.

The data for $H||b$ are shown in greater detail in Fig. 4(b), where P_aH_b and P_bH_b measured at 4.2 K are compared. For P_aH_b, a linear ME effect is observed at low fields, followed by a sudden drop at B_{SF}. It is worth noting, however, that

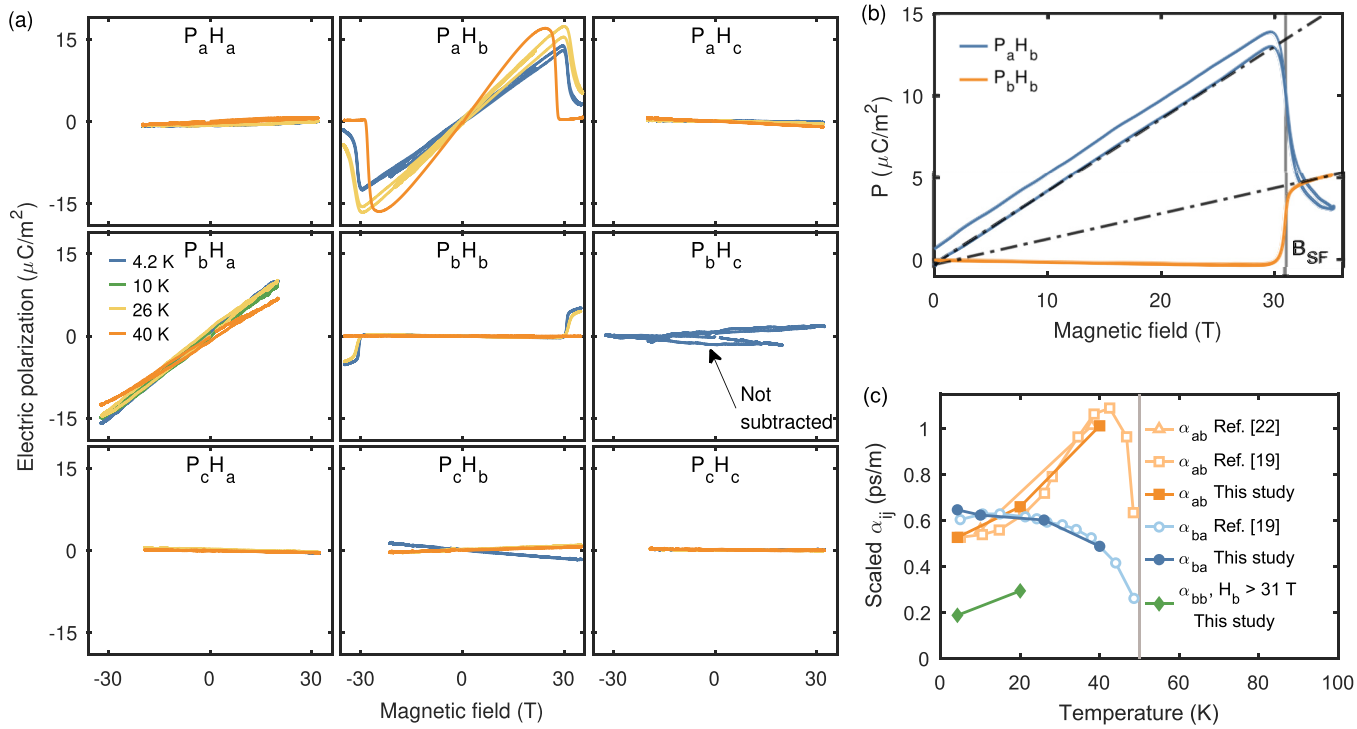

FIG. 4. Electric polarization P_i in applied pulsed magnetic fields H_j. Background measurements obtained at 60 K have been subtracted from all data, except P_bH_c, as explained in the text. (a) Overviewof all nine combinations of P_i and H_j for various temperatures. (b) Electric polarizations P_a and P_b as a function of magnetic fields applied along b clearly show the phase transition. The critical field $B_{SF} = 31$ T is indicated in by the gray vertical line. The dot-dashed lines represent linear fits to the polarization as a function of field to extract α_{ij}. (c) Temperature dependence of α_{ij}. Notice that the values obtained are merely proportional to α_{ij}. Our values are compared with scaled results from Refs. [19,22].

P_aH_b remains finite above the critical field. For P_bH_b, no ME signal is observed at low fields, but there is a steep increase at the transition whereafter a linear behavior with field is established up to the highest probed field strengths of 35 T.

The temperature dependence of the ME coefficients α_{ij} may be estimated from the experimentally determined electric polarization by fitting a linear function $P_i = P_0 + \alpha_{ij}H_j$ to the linear parts of the data in Fig. 4(a). The results obtained for the three finite tensor elements (α_{ba}, α_{ab}, and α_{bb}) are shown in Fig. 4(c). It should be noted that, while α_{ab} appears to be finite and nonzero above the phase transition, the field interval from B_{SF} to our maximum field is insufficient to distinguish if there is a linear or superlinear field dependence. It should be considered whether this finite α_{ab} could stem from a misalignment of the sample. However, assuming that the domain structure is comparable between measurements, a misalignment of the sample of $\approx 10^\circ$ would be needed to account for this nonzero signal in P_aH_b above B_{SF}. We are confident of the sample alignment within 5°, and hence, the finite P_aH_b above B_{SF} is most likely a real signal.

The ME coefficients for α_{ab} and α_{ba} in the low-field regime have previously been measured [19,22]. Figure 4(c) compares these results with our measurements. While, as already mentioned, the absolute values of α_{ij} cannot be compared directly, the temperature dependencies are still meaningful, and the values obtained for our unpoled setup are smaller than the literature values, as expected. Our temperature dependencies of α_{ab} and α_{ba} agree well with previously published results [19,22].

For the ME coefficients appearing for fields >31 T, we only have data at two temperatures. From these, it appears that α_{bb} in the high-field phase increases slightly with temperature but is otherwise lower than the ME coefficients present in the low-field phase.

We note also that, although a recent study found a weak but distinctly nonzero α_{aa} component in the low-field phase [22] for a poled $LiFePO_4$ sample, it is beyond our experimental limit to corroborate these findings. This is due to the experimental uncertainty connected to the pulsed-field technique as well as the fact that our sample is not poled. Without poling, multiple domains may be present, which will lower the measured polarization and therefore α_{ij} compared with poled measurements.

C. Possible field-induced spin canting

In both $LiNiPO_4$ and $LiCoPO_4$, a field-induced spin canting caused by the DM interaction occurs for magnetic fields applied in the transverse direction [15,44]. Measurements of the field dependence of relevant Bragg peaks reflecting such structure deviations have been used to estimate the strength of the DM interaction in these compounds. Likewise, here, we investigate whether any field-induced spin canting also occurs in $LiFePO_4$ and thus probe the strength of the DM interaction. We have probed five different Bragg peaks that reflect all

TABLE III. Squared structure factors (F^2) and polarization factors (P^2) and nuclear structure factors for Bragg reflections investigated with EIGER, see Eqs. (1)–(4).

q	$\|F_C\|^2$	$\|F_A\|^2$	$\|F_G\|^2$	$\|F_F\|^2$	$\|F_N\|^2$	$\|P_x\|^2$	$\|P_y\|^2$	$\|P_z\|^2$
(010)	16	0	0	0	0	1	0	1
(001)	0.29	0	16	0	0	1	1	0
(011)	0	16	0	0.29	260	1	0.62	0.38
(021)	0.29	0	16	0	0	1	0.29	0.71
(110)	0	0.49	16	0	0	0.75	0.25	1

possible field-induced cantings, as shown in Table III. The Bragg peaks (010), (001), (011), and (021) were investigated for fields along a, $B||a$, while the (110) peak was investigated for $B||c$. Figure 5 shows the difference in the neutron intensity for zero and finite magnetic fields. No intensity difference is observed for any of the peaks. This is in stark contrast with the Ni and Co compounds, where the intensity of the relevant Bragg peaks increases significantly in applied magnetic fields. This indicates a negligible DM interaction in $LiFePO_4$, to within the limits of sensitivity of the experiment.

V. DISCUSSION

A. Magnetic structure beyond 31 T

The appearance of the (030) Bragg peak >31 T in our pulsed-group symmetry $2_z/m'_z$. These observations rule out a possible C_z structure, and the only structure to satisfy both observations is a high-field phase with a dominant C_x structure and minor components C_y and A_z. This confirms the suggestion of a spin-flop transition put forward in Ref. [26], where the spins reorient from being predominantly along the b axis to being predominantly along the a axis with critical field $B_{SF} = 31$ T. Interestingly, this is the same point group as in the low-field phase but with a different distribution of the major and minor structure components. In the low-field phase, the system has major component C_y with minor C_x and A_z and a total spin canting away from b of 1.3(1)° [23]. In the high-field phase, the major component is now C_x and with smaller components of C_y and A_z. We cannot determine the relative weights of these smaller structure components in the high-field phase and thus cannot speculate on the size of the spin canting. However, such components may explain the anomalous magnetization curve above the critical field observed in Ref. [26]. Furthermore, magnetization measurements in the spin-flop phase [26,28] show a magnetization jump to $\approx\frac{1}{2}$ of the saturation magnetization at the spin-flop transition, meaning that a sizable F_y component has been induced. The resulting inferred spin-flop structure is illustrated in Fig. 6(b) for a magnetic field immediately above the transition. The magnetic structures below and above the transition are illustrated in Figs. 6(a) and 6(b).

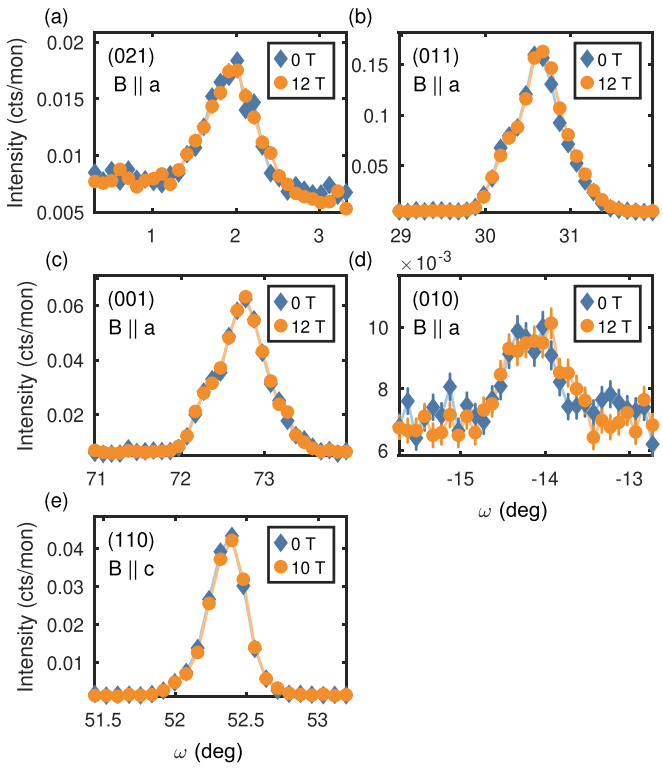

FIG. 5. Sample rotation ω scan of different Bragg peaks at low and high magnetic fields. All scans were performed at 2 K. Scans (a)–(d) are with magnetic fields along a, while scan (e) is with field along c.

B. Phase diagram and Hamiltonian

Figure 6(c) shows the phase diagram obtained of $LiFePO_4$ by combining the magnetization measurements from Refs. [26,28] with our neutron diffraction and electric polarization measurements. Based on anomalies in the magnetization, Werner *et al.* [26] reported a precursor phase just below the spin-flop transition at 1.5 K. We see no evidence of the AFM′ phase in the electric polarization measurements down to 4.2 K. The magnetic structure has now been established in both the low-field phase (cf. Ref. [23]) and the high-field phase (this paper). Combined with the realization that the DM interaction is of negligible size, based on the lack of any field-induced spin canting as seen in our neutron diffraction measurements, we now try to consolidate our understanding of $LiFePO_4$ by use of MF calculations.

The Hamiltonian of $LiFePO_4$ can be written as $\hat{\mathcal{H}} = \frac{1}{2}\sum_{ij} J_{ij}\,\mathbf{S}_i \cdot \mathbf{S}_j + \sum_{\alpha,i} \mathfrak{D}_\alpha (S_i^\alpha)^2$, where J_{ij} are the Heisenberg exchange interactions, and $\mathfrak{D}_\alpha$ is the single-ion anisotropy constant for $\alpha = \{a, b, c\}$ [8,23,28]. A number of different estimates of the exchange interactions and anisotropies of $LiFePO_4$ have been published [8,12,23,27,28]. However, of these studies, only Refs. [8,23] incorporate all the leading exchange interactionsand assume the DM interaction to be negligible. In Refs. [8,23], the couplings were obtained from fitting dispersion relations from linear spin-wave theory to the excitation spectrum measured by neutron spectroscopy. One notable difference between the two studies is that the estimate of Ref. [8] renders $LiFePO_4$ more frustrated in the (b, c) plane than Ref. [23] and with a larger value of the single-ion anisotropy $\mathfrak{D}_c$.

Using these two sets of parameters, we calculated the phase diagram and magnetic structures using a MF calculation as implemented in the program McPhase [45]. The calculations

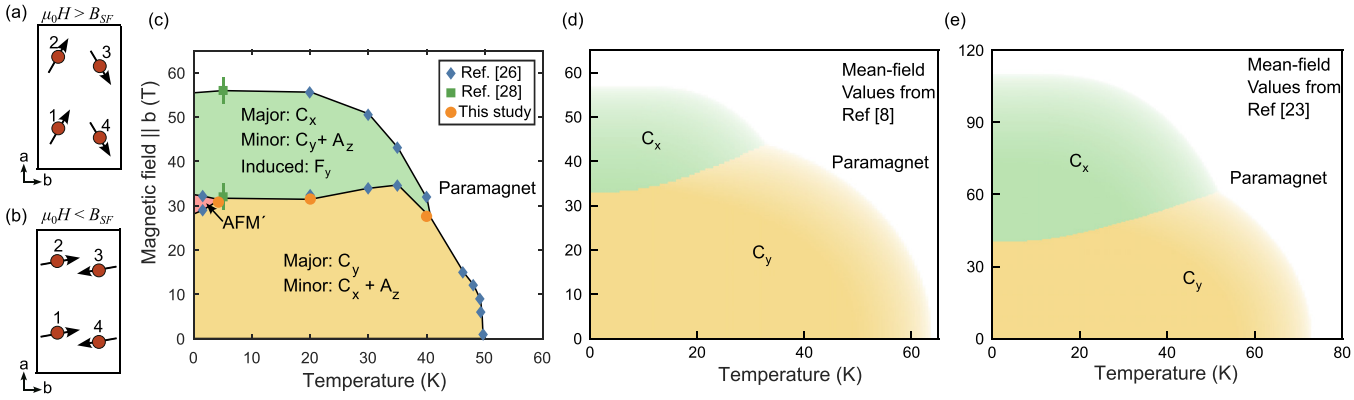

FIG. 6. Magnetic structures of $LiFePO_4$ in (a) the spin-flop and (b) the low-field phase. (c) Experimental phase diagram of $LiFePO_4$ for magnetic fields along *b*. Figure includes results from our neutron diffraction and electric polarization measurements as well as magnetization data from Refs. [26,28]. (d) and (e) Phase diagrams as determined from mean-field calculations with two different sets of parameters [8,23].

consider only the spin moments. We find an insignificant difference if we include the orbital moments and the full crystal field Hamiltonian as was used by Ref. [8], with a slightly lower spin-flop and saturation fields and lower T_N. The resulting phase diagrams are shown in Figs. 6(d) and 6(e). For both sets of parameters, we find C_y AFM order at low temperatures and low fields, as well as a spin-flop transition to C_x AFM order at elevated fields before saturation is reached at yet higher fields. We note that neither set of exchange couplings predict any AFM′ phase at low temperature, as observed in Ref. [26].

It is evident when comparing Figs. 6(a) and 6(d) that the phase diagram for the values in Ref. [8] match the experimental phase diagram well. In fact, the spin-flop and saturation fields obtained using the exchange and anisotropy parameters from Ref. [8] are within ∼5% of the experimental values, while the critical fields for the parameters from Ref. [23] are significantly higher. The Néel temperatures and spin-flop and saturations fields obtained from the MF calculations are summarized in Table IV and compared with the experimental values. Thus, we conclude that the parameters obtained by Yiu *et al.* [8] provide a better description of the phase diagram of $LiFePO_4$.

With regard to the DM interaction, $LiFePO_4$ seems to be distinct from the two relevant family members $LiNiPO_4$ and $LiCoPO_4$ with much smaller zero-field canting. ESR [27] and terahertz [28] spectroscopy estimate the DM interaction to be <0.05 meV, and our neutron diffraction results confirm this, using the same method of investigation used on the other two family members. This is significantly smaller than the DM interactions in the Ni and Co compounds, being 0.4 meV [31] and 0.7 meV [44], respectively. The *Pnma*-allowed DM interaction has the form $\hat{\mathcal{H}}_{\rm DM} = D^b_{12}(S^z_1 S^x_2 - S^x_1 S^z_2) + D^b_{34}(S^z_3 S^x_4 - S^x_3 S^z_4)$. However, the distorted octahedra surrounding the magnetic ions give rise to a low crystal-ion terms of the form [15] $\hat{\mathcal{H}}_{\mathfrak{D}} = -\mathfrak{D}_{xz}(S^z_1 S^x_1 - S^x_2 S^z_2 + S^z_3 S^x_3 - S^x_4 S^z_4)$. The two terms have a similar origin as higher order orbital processes, and are hard to distinguish experimentally.

TABLE IV. Sets of estimated exchange interactions and single-ion anisotropies (in meV) from previous publications [8,23]. Also shown are the predicted MF values of critical temperature and fields at 4 K [see Figs. 6(d) and 6(e)] compared with the experimental values.

	Toft-Petersen *et al.* (2015) [23]	Yiu *et al.* (2017) [8]	
J_{bc}	0.77(2)	0.46(2)	
J_b	0.30(2)	0.09(1)	
J_c	0.14(2)	0.01(1)	
J_{ab}	0.14(2)	0.09(1)	
J_{ac}	0.05(1)	0.01(1)	
$\mathfrak{D}_a$	0.62(1)	0.86(2)	
$\mathfrak{D}_c$	1.56(4)	2.23(2)	
	MF theory		Measured
T_N (K)	73	62	50
$B_{\rm SF}$ (T)	40	33	31
$B_{\rm Sat}$ (T)	110	57	56

VI. CONCLUSIONS

Motivated by the discovery of a phase transition in $LiFePO_4$ at high fields along the crystallographic *b* axis [26], we have combined pulsed-field neutron diffraction and electric polarization measurements. Our results show that the phase transition is of the spin-flop type with $B_{\rm SF} = 31$ T at 4 K. Above the transition, a ME active phase exists with finite α_{bb} and α_{ba} ME tensor elements. By combining the results from pulsed-field neutron diffraction and electric polarization measurements, we argue that the high-field AFM structure is dominantly C_x with magnetic moments along the *a* axis but also that further subdominant C_y and A_x components are required to explain the nonzero α_{ba}. This indicates a lower-symmetry magnetic point group than a simple spin-flop phase. Furthermore, neutron diffraction experiments in magnetic fields along *c* and *a* showed no field-induced spin canting in $LiFePO_4$, which demonstrates a DM interaction of negligible strength. Phase diagrams calculated using MF theory indicate that the coupling parameters determined by Yiu *et al.* [8] match well the observations for $LiFePO_4$.

ACKNOWLEDGMENTS

We thank Lise Grüner Hanson (DTU Physics) for help with conducting the EIGER neutron experiments. This project was supported by a research grant (No. 35921) from VILLUM FONDEN as well as the European Research Council through the Synergy network HERO (Grant No. 810451) and the Swiss National Science Foundation through Project Grant No. 188648. The neutron experiment at the Materials and Life Science Experimental Facility of the J-PARC was performed under a user program (Proposal No. 2021B0166). The other neutron experiment was performed at the Swiss spallation neutron source SINQ, Paul Scherrer Institute, Villigen, Switzerland. Polarization measurements were performed at the Institute for Solid State Physics, Japan. R.T.P. was supported by GIMRT and ICC-IMR. D.V. and J. L. grew and characterized the crystals. Their research was supported by the U.S. Department of Energy(DOE), Office of Basic Energy Sciences, Division of Materials Sciences and Engineering. Ames National Laboratory is operated for the DOE by Iowa State University under Contract No. DE-AC02-07CH11358. The experimental work was supported by the instrument center DanScatt funded through the Danish Agency for Science, Technology, and Innovation through Grant No. 7129-00003B.

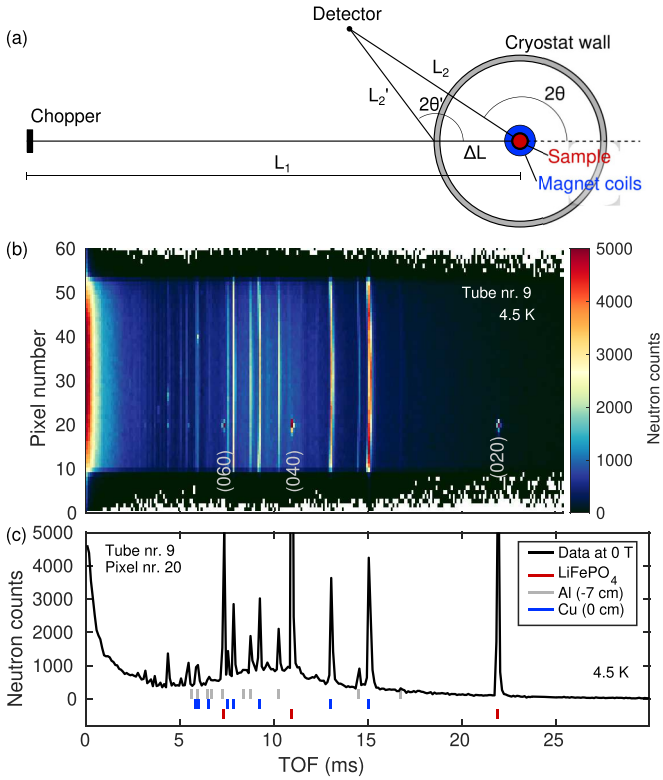

FIG. 7. Identification of powder lines arising from the sample environment (cryostat wall and magnet coils) and nuclear Bragg peaks from the sample. (a) Experimental geometry showing the position of the cryostat wall, magnet coils, and sample. Note that the sketch is not to scale. (b) Neutron diffraction data collected at zero field as a function of pixel number and time of flight(ToF) for detector tube No. 9. Color contours represent the neutron counts. Nuclear Bragg peaks (020), (040), and (060) are observed as high-intensity spots around pixel No. 20. Powder lines have intensity spread out homogeneously over all pixels. (c) Neutron counts as a function of ToF collected at zero field and 4.5 K in detector tube No. 9 and pixel No. 20. Nuclear Bragg peak positions from the sample are marked with red lines. Powder lines from the cryostat wall (aluminum) and magnet coils (copper) are marked with, respectively, gray and blue lines.

APPENDIX A: POWDER LINES AND BACKGROUND AT NOBORU

In addition to the Bragg peaks arising from $LiFePO_4$, our pulsed-field neutron diffraction data contained multiple additional high-intensity peaks. To investigate the origin of these features, we considered scattering from the sample surroundings. Two main sources of polycrystalline elastic scattering were identified: the cryostat wall in aluminum and the magnet coils in copper, positioned as shown in Fig. 7(a). The quantities indicated in the sketch are $L_1 = 14\,\text{m}$, $L_2 = 0.9\,\text{m}$,

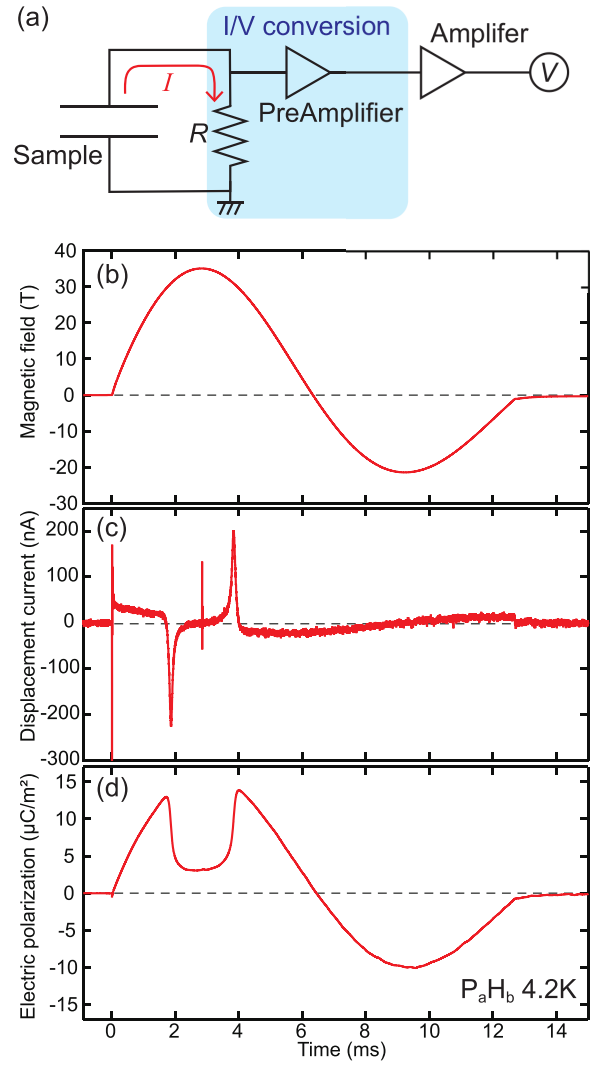

FIG. 8. (a) Experimental setup for polarization measurement. (b) Two consecutive magnetic field pulse of duration 6.1 ms. (c) The measured displacement current during the time of the pulse. (d) The deduced electric polarization. As evident, the electric polarization along *a* has a plateau in the spin flop phase, for field applied along the *b* axis, as discussed in the main text.

$2\theta = 150^\circ$, and ΔL in the range $[-15, 0]$ cm, where negative ΔL corresponds to a position before the sample. Bragg peaks from the sample are distinguished from the powder lines as high-intensity spots on the detector, see Fig. 7(b). The cryostat contains several aluminum shields, but most peaks in the diffraction pattern are well accounted for by including a single wall of aluminum positioned 7 cm before the sample and copper at the sample position as shown in Fig. 7(c), considering the second cryostat wall after the sample does not yield any additional insight. Most important for our data analysis is the identification of the lines ∼15 ms, which are close to the location of the (030) Bragg peak. It is clear that these arise from the sample environment, and any additional intensity in this area at high magnetic fields must find its origin in the sample itself.

APPENDIX B: POLARIZATION MEASUREMENTS

Lastly, we elaborate on the pulsed-crystal plate is connected to two electrodes, and as the magnetic field changes with time, the ME effect induces a change in bulk polarization and thereby a change in the surface charge on the electrodes. This gives rise to a so-called displacement current in the circuit. A diagram of the circuit is given in Fig. 8(a). For I/V conversion, a LI-76 converter from the NF Corporation was used, and the low-noise voltage preamplifier was a SR560 model from Stanford Research Systems. For obtaining the electric polarization, the displacement current is integrated over time:

$$\begin{aligned} P(T_1) &= P(T_0) - \frac{1}{A}\int_{T_0}^{T_1} I(T)dT \\ &= P(T_0) - \frac{1}{A}\int_{T_0}^{T_1} \frac{V(T)}{R}dT, \end{aligned} \tag{B1}$$

where $I(T)$ and $V(T)$ are the current and voltage, respectively, A is the crystal electrode area, and R is the resistance.

[1] S. Manipatruni, D. E. Nikonov, C. C. Lin, T. A. Gosavi, H. Liu, B. Prasad, Y. L. Huang, E. Bonturim, R. Ramesh, and I. A. Young, Scalable energy-efficient magnetoelectric spin-orbit logic, Nature (London) **565**, 35 (2019).

[2] F. Trier, P. Noël, J.-V. Kim, J.-P. Attané, L. Vila, and M. Bibes, Oxide spin-orbitronics: Spin-charge interconversion and topological textures, Nat. Rev. Mater. **7**, 258 (2022).

[3] M. Fiebig, T. Lottermoser, D. Meier, and M. Trassin, The evolution of multiferroics, Nat. Rev. Mater. **1**, 16046 (2016).

[4] N. A. Spaldin and R. Ramesh, Advances in magnetoelectric multiferroics, Nat. Mater. **18**, 203 (2019).

[5] X. Liang, A. Matyushov, P. Hayes, V. Schell, C. Dong, H. Chen, Y. He, A. Will-Cole, E. Quandt, P. Martins *et al.*, Roadmap on magnetoelectric materials and devices, IEEE Trans. Magn. **57**, 1 (2021).

[6] Y. Ba, S. Zhuang, Y. Zhang, Y. Wang, Y. Gao, H. Zhou, M. Chen, W. Sun, Q. Liu, G. Chai *et al.*, Electric-field control of skyrmions in multiferroic heterostructure via magnetoelectric coupling, Nat. Commun. **12**, 322 (2021).

[7] J. P. Rivera, A short review of the magnetoelectric effect and related experimental techniques on single phase (multi-) ferroics, Eur. Phys. J. B **71**, 299 (2009).

[8] Y. Yiu, M. D. Le, R. Toft-Petersen, G. Ehlers, R. J. McQueeney, and D. Vaknin, Hybrid excitations due to crystal field, spin-orbit coupling, and spin waves in $LiFePO_4$, Phys. Rev. B **95**, 104409 (2017).

[9] G. Quirion and M. L. Plumer, Landau theory of the magnetic phase diagram of monoclinic multiferroics: Application to $MnWO_4$ and CuO, Phys. Rev. B **87**, 174428 (2013).

[10] M. Mercier, Étude de l'effet magnetoelectrique sur de composés de type olivine, perovskite et grenat, Ph.D. thesis, Université de Grenoble, 1969.

[11] R. P. Santoro and R. E. Newnham, Antiferromagnetism in $LiFePO_4$, Acta Cryst. **22**, 344 (1967).

[12] J. Li, V. O. Garlea, J. L. Zarestky, and D. Vaknin, Spin-waves in antiferromagnetic single-crystal $LiFePO_4$, Phys. Rev. B **73**, 024410 (2006).

[13] E. Fogh, R. Toft-Petersen, E. Ressouche, C. Niedermayer, S. L. Holm, M. Bartkowiak, O. Prokhnenko, S. Sloth, F. W. Isaksen, D. Vaknin *et al.*, Magnetic order, hysteresis, and phase coexistence in magnetoelectric $LiCoPO_4$, Phys. Rev. B **96**, 104420 (2017).

[14] R.P. Santoro, D.J. Segal, and R.E. Newnham, Magnetic properties of $LiCoPO_4$ and $LiNiPO_4$, J. Phys. Chem. Solids **27**, 1192 (1966).

[15] T. B. S. Jensen, N. B. Christensen, M. Kenzelmann, H. M. Rønnow, C. Niedermayer, N. H. Andersen, K. Lefmann, J. Schefer, M. v. Zimmermann, J. Li *et al.*, Field-induced magnetic phases and electric polarization in $LiNiPO_4$, Phys. Rev. B **79**, 092412 (2009).

[16] D. Vaknin, J. L. Zarestky, J.-P. Rivera, and H. Schmid, Antiferromagnetism in $LiCoPO_4$ and $LiNiPO_4$, in *Magnetoelectric Interaction Phenomena in Crystals*, NATO Science Series, edited by M. Fiebig, V. V. Eremenko, and I. E. Chupis (Springer, Dordrecht, 2004), Vol. 164, pp. 203–217.

[17] G. Rousse, J. Rodriguez-Carvajal, S. Patoux, and C. Masquelier, Magnetic structures of the triphylite $LiFePO_4$ and of its delithiated form $FePO_4$, Chem. Mater. **15**, 4082 (2003).

[18] R. Toft-Petersen, N. H. Andersen, H. Li, J. Li, W. Tian, S. L. Bud'ko, T. B. S. Jensen, C. Niedermayer, M. Laver, O. Zaharko *et al.*, Magnetic phase diagram of magnetoelectric $LiMnPO_4$, Phys. Rev. B **85**, 224415 (2012).

[19] M. Mercier, P. Bauer, and B. Fouilleux, Mesures magnétoélectriques sur $LiFePO_4$, C. R. Acad. Sci. Paris B **267**, 1345 (1968).

[20] E. Fogh, B. Klemke, M. Reehuis, P. Bourges, C. Niedermayer, S. Holm-Dahlin, O. Zaharko, J. Schefer, A. B. Kristensen, M. K. Sørensen *et al.*, Tuning magnetoelectricity in a mixed-anisotropy antiferromagnet, Nat. Commun. **14**, 3408 (2023).

[21] E. Fogh, T. Kihara, R. Toft-Petersen, M. Bartkowiak, Y. Narumi, O. Prokhnenko, A. Miyake, M. Tokunaga, K. Oikawa, M. K. Sørensen *et al.*, Magnetic structures and quadratic magnetoelectric effect in $LiNiPO_4$ beyond 30 T, Phys. Rev. B **101**, 024403 (2020).

[22] E. Fogh, B. Klemke, A. Pages, J. Li, D. Vaknin, H. M. Rønnow, N. B. Christensen, and R. Toft-Petersen, The magnetoelectric effect in $LiFePO_4$—Revisited, Physica B: Condens. Matter **648**, 414380 (2023).

[23] R. Toft-Petersen, M. Reehuis, T. B. S. Jensen, N. H. Andersen, J. Li, M. D. Le, M. Laver, C. Niedermayer, B. Klemke, K. Lefmann *et al.*, Anomalous magnetic structure and spin dynamics in magnetoelectric $LiFePO_4$, Phys. Rev. B **92**, 024404 (2015).

[24] T. B. S. Jensen, N. B. Christensen, M. Kenzelmann, H. M. Rønnow, C. Niedermayer, N. H. Andersen, K. Lefmann, M. Jiménez-Ruiz, F. Demmel, J. Li *et al.*, Anomalous spin waves and the commensurate-incommensurate magnetic phase transition in $LiNiPO_4$, Phys. Rev. B **79**, 092413 (2009).

[25] A. Scaramucci, E. Bousquet, M. Fechner, M. Mostovoy, and N. A. Spaldin, Linear magnetoelectric effect by orbital magnetism, Phys. Rev. Lett. **109**, 197203 (2012).

[26] J. Werner, S. Sauerland, C. Koo, C. Neef, A. Pollithy, Y. Skourski, and R. Klingeler, High magnetic field phase diagram and failure of the magnetic Grüneisen scaling in $LiFePO_4$, Phys. Rev. B **99**, 214432 (2019).

[27] J. Werner, C. Neef, C. Koo, A. Ponomaryov, S. Zvyagin, and R. Klingeler, Exceptional field dependence of antiferromagnetic magnons in $LiFePO_4$, Phys. Rev. B **103**, 174406 (2021).

[28] L. Peedu, V. Kocsis, D. Szaller, B. Forrai, S. Bordács, I. Kézsmárki, J. Viirok, U. Nagel, B. Bernáth, D. L. Kamenskyi *et al.*, Terahertz spectroscopy of spin excitations in magnetoelectric $LiFePO_4$ in high magnetic fields, Phys. Rev. B **106**, 134413 (2022).

[29] J. Li, W. Tian, Y. Chen, J. L. Zarestky, J. W. Lynn, and D. Vaknin, Antiferromagnetism in the magnetoelectric effect single crystal $LiMnPO_4$, Phys. Rev. B **79**, 144410 (2009).

[30] D. Vaknin, J. L. Zarestky, J. P. Rivera, and H. Schmid, Commensurate-incommensurate magnetic phase transition in magnetoelectric single crystal $LiNiPO_4$, Phys. Rev. Lett. **92**, 207201 (2004).

[31] R. Toft-Petersen, J. Jensen, T. B. S. Jensen, N. H. Andersen, N. B. Christensen, C. Niedermayer, M. Kenzelmann, M. Skoulatos, M. D. Le, K. Lefmann *et al.*, High-field magnetic phase transitions and spin excitations in magnetoelectric $LiNiPO_4$, Phys. Rev. B **84**, 054408 (2011).

[32] K. Kuwahara, S. Yoshii, H. Nojiri, D. Aoki, W. Knafo, F. Duc, X. Fabrèges, G. W. Scheerer, P. Frings, G. L. J. A. Rikken *et al.*, Magnetic structure of phase II in $\mathbf{U}(Ru_{0.96}Rh_{0.04})_2Si_2$ determined by neutron diffraction under pulsed high magnetic fields, Phys. Rev. Lett. **110**, 216406 (2013).

[33] H. Nojiri, S. Yoshii, M. Yasui, K. Okada, M. Matsuda, J. S. Jung, T. Kimura, L. Santodonato, G. E. Granroth, K. A. Ross *et al.*, Neutron laue diffraction study on the magnetic phase diagram of multiferroic $MnWO_4$ under pulsed high magnetic fields, Phys. Rev. Lett. **106**, 237202 (2011).

[34] S. Yoshii, K. Ohoyama, K. Kurosawa, H. Nojiri, M. Matsuda, P. Frings, F. Duc, B. Vignolle, G. L. J. A. Rikken, L.-P. Regnault *et al.*, Neutron diffraction study on the multiple magnetization plateaus in TbB_4 under pulsed high magnetic field, Phys. Rev. Lett. **103**, 077203 (2009).

[35] F. Duc, X. Fabrèges, T. Roth, C. Detlefs, P. Frings, M. Nardone, J. Billette, M. Lesourd, L. Zhang, A. Zitouni *et al.*, A 31 T split-pair pulsed magnet for single crystal x-ray diffraction at low temperature, Rev. Sci. Instrum. **85**, 053905 (2014).

[36] K. Ohoyama, N. Katoh, H. Nojiri, Y. Matsuda, H. Hiraka, K. Ikeda, and H. Shimizu, Neutron diffraction under 30 T pulsed magnetic fields, J. Magn. Magn. Mater. **310**, e974 (2007).

[37] A. Gazizulina, D. L. Quintero-Castro, Z. Wang, F. Duc, F. Bourdarot, K. Prokes, W. Schmidt, R. Daou, S. Zherlitsyn, N. Islam *et al.*, Neutron diffraction of field-induced magnon condensation in the spin-dimerized antiferromagnet $Sr_3Cr_2O_8$, Phys. Rev. B **104**, 064430 (2021).

[38] F. Duc, X. Tonon, J. Billette, B. Rollet, W. Knafo, F. Bourdarot, J. Béard, F. Mantegazza, B. Longuet, J. E. Lorenzo *et al.*, 40-Tesla pulsed-field cryomagnet for single crystal neutron diffraction, Rev. Sci. Instrum. **89**, 053905 (2018).

[39] R. Toft-Petersen, E. Fogh, T. Kihara, J. Jensen, K. Fritsch, J. Lee, G. E. Granroth, M. B. Stone, D. Vaknin, H. Nojiri *et al.*, Field-induced reentrant magnetoelectric phase in $LiNiPO_4$, Phys. Rev. B **95**, 064421 (2017).

[40] K. Oikawa, F. Maekawa, M. Harada, T. Kai, S. Meigo, Y. Kasugai, M. Ooi, K. Sakai, M. Teshigawara, S. Hasegawa *et al.*, Design and application of NOBORU-neutron beam line for observation and research use at J-PARC, Nucl. Instrum. Methods Phys. Res. A **589**, 310 (2008).

[41] M. Watanabe, T. Kihara, and H. Nojiri, Automated pulsed magnet system for neutron diffraction experiments at the materials and life science experimental facility in J-PARC, Quantum Beam Sci. **7**, 1 (2023).

[42] U. Stuhr, B. Roessli, S. Gvasaliya, H. M. Rønnow, U. Filges, D. Graf, A. Bollhalder, D. Hohl, R. Bürge, M. Schild *et al.*, The thermal triple-axis-spectrometer EIGER at the continuous spallation source SINQ, Nucl. Instrum. Methods Phys. Res. A **853**, 16 (2017).

[43] J. Werner, C. Neef, C. Koo, S. Zvyagin, A. Ponomaryov, and R. Klingeler, Antisite disorder in the battery material $LiFePO_4$, Phys. Rev. Mater. **4**, 115403 (2020).

[44] E. Fogh, O. Zaharko, J. Schefer, C. Niedermayer, S. Holm-Dahlin, M. K. Sørensen, A. B. Kristensen, N. H. Andersen, D. Vaknin, N. B. Christensen *et al.*, Dzyaloshinskii-Moriya interaction and the magnetic ground state in magnetoelectric $LiCoPO_4$, Phys. Rev. B **99**, 104421 (2019).

[45] M. Rotter, Using McPhase to calculate magnetic phase diagrams of rare earth compounds, J. Magn. Magn. Mater. **272-276**, E481 (2004).